Nano Energy 70 (2020) 104519

Contents lists available at ScienceDirect

Nano Energy

journal homepage: http://www.elsevier.com/locate/nanoen

Full paper

Fast and reversible zinc ion intercalation in Al-ion modified hydrated vanadate

Jiqi Zheng [a,b,1], Chaofeng Liu [a,1], Meng Tian [a], Xiaoxiao Jia [a], Evan P. Jahrman [c], Gerald T. Seidler [c], Shaoqing Zhang [d], Yanyan Liu [b], Yifu Zhang [b,**], Changgong Meng [b], Guozhong Cao [a,*]

[a] Department of Materials Science and Engineering, University of Washington, Seattle, WA, 98195, USA
[b] School of Chemical Engineering, Dalian University of Technology, Dalian, 116024, PR China
[c] Physics Department, University of Washington, Seattle, WA, 98195-1560, United States
[d] Anhui Science and Technology University, Chuzhou, 239000, PR China

ARTICLE INFO

Keywords:
Zinc ion batteries
Hydrated vanadium oxides
Aluminum ion introduction
Expanded lattice spacing

ABSTRACT

Aqueous Zn-ion batteries (ZIBs) are emerging candidates for safe and eco-friendly large-scale energy storage, but the critical challenge is to develop stable and robust cathode materials for reversible and fast Zn^{2+} intercalation. In the present work, the drawbacks of pure hydrated vanadium oxides (VOH), including low ion mobility and cycling instability, are mitigated by modifying the local atomic environment and increasing the amount of tetravalent vanadium cations. These effects are achieved by introducing trivalent Al-ions during a one-step hydrothermal synthesis. The expanded lattice spacing and improved conductivity of the synthesized Al–VOH enable rapid Zn^{2+} diffusion and electron transfer, leading to a high capacity of 380 mAh·g^{-1} at 50 mA g^{-1}, as well as the excellent long-term cycling stability (capacity maintained over 3000 cycles). Further investigations of the reaction kinetics and mechanism reveal the effects of introducing Al-ions, and the role of Zn^{2+} trapped upon initial charging plays in promoting the subsequent electrochemical process and preventing the structural degradation.

1. Introduction

Electrochemical energy storage devices play an indispensable role in the efficient utilization of intermittent renewable energy sources such as wind, solar and tidal energy [1–4]. Li-ion batteries (LIBs) have been extensively exploited and commercialized during the past three decades owing to their light weight and high energy density [5,6]. However, economic and safety concerns have motivated a search for other reliable and high-efficiency alternatives [7–9]. Aqueous rechargeable batteries employing multivalent-ions such as Zn^{2+}, Ca^{2+}, Mg^{2+} and Al^{3+} are considered promising candidates due to the high safety and ionic conductivities of aqueous electrolytes, as well as the high energy density achieved by employing the multi-electron redox reactions [10–12]. Among them, Zn-ion batteries (ZIBs) are appealing as they are eco-friendly, non-toxic, and already have a suitable negative anode material [13–17]. The advantages of Zn metal include high volumetric capacity (5855 mAh·cm^{-3}), low redox potential (−0.76 V vs. standard hydrogen electrode) which enables an appropriate operating voltage in aqueous electrolytes, low cost and high safety, making it an ideal anode material for ZIBs [18–20]. Thus the development of high-performance cathode materials is becoming the primary challenge for the commercialization of ZIBs.

V-based oxides have received tremendous attention among the numerous proposed ZIB cathode materials, which also include Mn-based oxides, Mo-based sulfides, and Prussian blue analogs [7,21,22]. The V-based oxides are advantageous because of their abundance, typical layered-crystal structure that allows efficient Zn^{2+} intercalation, and multiple valence states contributing to a high specific capacity [23–25]. Nonetheless, though pure V oxides such as V_2O_5 have moderate electronic conductivity, the formation of soluble species and crystal

* Corresponding author.
** Corresponding author.
E-mail addresses: yfzhang@dlut.edu.cn (Y. Zhang), gzcao@uw.edu (G. Cao).
[1] J. Z. and C. L. contributed equally.

https://doi.org/10.1016/j.nanoen.2020.104519
Received 2 September 2019; Received in revised form 27 November 2019; Accepted 18 January 2020
Available online 21 January 2020
2211-2855/Published by Elsevier Ltd.

structure degradation during the continuous intercalation/deintercalation of Zn^{2+} hinder their long-cycling stability and the commercial practicality [26–28]. Recent research demonstrated the crucial role of structural water, which serves as pillars to maintain structural stability and decreases the effective charge repulsion of Zn^{2+} and, thus, improves the electrochemical performance of V oxides [29, 30]. Introducing cation-pillars between layered vanadium oxides is another effective and efficient strategy [31]. Since $Zn_{0.25}V_2O_5{\cdot}nH_2O$ works for ZIBs with a high capacity of 282 $mAh{\cdot}g^{-1}$ at 1C and satisfactory cycling stability [32], a series of hydrated vanadates, such as $Ca_{0.25}V_2O_5{\cdot}nH_2O$ [10], $NaV_3O_8{\cdot}1.5H_2O$ [33], $Mg_xV_2O_5{\cdot}nH_2O$ [34], $Na_2V_6O_{16}{\cdot}3H_2O$ [35] and $Na_2V_6O_{16}{\cdot}1.63H_2O$ [36] have been also synthesized and delivered competitive electrochemical properties, indicating introducing cations and water molecules into the slabs of V-based oxides can effectively stabilize the crystal structures and enhance their performances as cathodes for ZIBs. It has been recently demonstrated that expanding the interplanar spacing of hydrated vanadate by introducing Mn(II) ions (MnVO) resulted in the cathode material becoming more thermodynamically and structurally stable. MnVO exhibited an excellent Zn-ion intercalation due to its fast ion diffusion and enhanced electrical conductivity [37]. As the alkali, alkaline earth and transition metals reported so far are mainly monovalent or divalent [20], studying the effects of trivalent ions constitutes a meaningful addition to the field. As the most abundant metallic element in the Earth's crust (8.3 wt% in the Earth's crust) [38], aluminum contains the merits of low cost and low toxicity compared with transition metals. The trivalent Al-ions form stable chemical bonds with O atoms in the VO_x slabs with a Al–O bond energy of 502 kJ mol^{-1}, which is greater than those reported for Na–O (270 kJ mol^{-1}), Mg–O (358 kJ mol^{-1}), and Mn–O (362 kJ mol^{-1}) [39]. Unlike transition metal ions, the empty d orbitals and the stable valence state of Al^{3+} minimize the effect of the introduced ions have on the electrochemical process. These merits make Al an ideal element for improving electrochemical properties of hydrated vanadates and revealing the effects of introducing cations. Recently, Li et al. reported the Al-doped $V_{10}O_{24}{\cdot}12H_2O$ cathode material for ZIBs, which exhibited an improved cycling stability compared with pure $V_{10}O_{24}{\cdot}12H_2O$. However, the doping of Al^{3+} did not have effect on the crystal structure especially the interlayer spacing, and a lower initial capacity after doping was delivered [40]. Zhang et al. also synthesized pure $H_{11}Al_2V_6O_{23.2}$ nanobelts and their composite with graphene, which had a large interlayer spacing of 13.36 Å. Both materials showed similar specific capacities, but the cycling stability of pure $H_{11}Al_2V_6O_{23.2}$ was unsatisfied and needed to be improved by the coating of graphene [41]. These results proved that the introduction of Al element can improve the cycling stability and capacity, thus exploiting V oxide-based cathode materials with improved capacity and high cycling stability by introducing Al^{3+} is realizable.

In the present work, Al-ions were introduced into hydrated vanadium oxides (Al–VOH) for highly reversible Zn-ion intercalation, but it has totally different crystal structure compared to the abovementioned samples contained Al dopant. Characterizations of Al–VOH indicate a nanostructured morphology and an enlarged interlayer spacing. Furthermore, pairing a Zn metal anode with an Al–VOH cathode resulted in a highly reversible redox reaction and a high cycling stability, as confirmed by electrochemical measurements. Additional characterizations of the electrode material, including XRD, XPS, EDS, ICP, and XANES, reveal the energy storage mechanism. The results revealed that the expanded lattice spacing of Al–VOH enables fast ion migration, and that the introduction of V^{4+} is beneficial for charge transfer. It is noteworthy that the Zn^{2+} trapped upon initial can promote the subsequent redox processes and assist in stabilizing the structure together with the Al-ions. The above properties of Al–VOH result in a high capacity of 380 $mAh{\cdot}g^{-1}$ at 50 mA g^{-1} while maintaining a long-term cycling stability (the capacity did not decrease after 3000 cycles at 4 A g^{-1}), making it a promising cathode material for high-performance aqueous ZIBs.

2. Material and methods

2.1. Synthesis of Al–VOH

Al–VOH was synthesized by a one-step hydrothermal reaction. In detail, 0.364 g V_2O_5 (99.6%, Sigma-Aldrich) along with 2 mL H_2O_2 (30%, Fisher Chemical) was dispersed in 50 mL D.I. water, in which the solution of 0.171 g $Al_2(SO_4)_3{\cdot}xH_2O$ (x = 14–18, 98–102%, Alfa Aesar) dissolved in 30 mL D.I. water was added. The mixture was transferred into a 100 mL Teflon-lined stainless-steel autoclave after stirring and heated at 120 °C for 6 h. The obtained dark red precipitate was centrifuged, washed with water and ethanol for three times. The product was dried in an oven at 70 °C for 12 h first, then further dried in vacuum at 120 °C. For comparison, pure $V_2O_5{\cdot}1.6\ H_2O$ was synthesized in the same hydrothermal process, just without the Al source, and was dried through freeze drying.

2.2. Material characterizations

X-ray diffraction (XRD) was used to identify the compositions and structures of the products using Bruker D8 Discover X-ray diffractometer with an ImS 2-D detection system (50 kV, 1000 mA). Raman spectra were recorded on a Renishaw InVia Raman microscope with a laser excitation sources of 514 nm. Fourier transform infrared spectroscopy (FTIR) spectra were collected on a Nicolet 6700 spectrometer from 4000 to 400 cm^{-1} using the KBr pellet technique. X-ray photoelectron spectrum (XPS) was taken on a Thermo ESCALAB 250XiX spectrometer with monochromatized Al Kα X-ray ($h\nu$ = 1486.6 eV). Inductively Coupled Plasma (ICP, PerkinElmer, Optima2000DV) was adopted to analyze the content of metal elements. X-ray absorption near-edge structure (XANES) measurements were performed at the vanadium K-edge using a laboratory-based instrument using the reported methodology [42–44]. A linear relationship was assumed between the edge position and oxidation state. The average oxidation of V in samples was determined by fitting a linear function to the rising edge (around 5474–5484 eV) of the normalized XANES spectrum. The energy which corresponded to an absorption intensity of half the edge step was then used to determine the proportion of V^{4+} and V^{5+} atoms by comparison to V oxides which served as empirical standards. The microstructures and chemical compositions of the products were characterized by a field-emission scanning electron microscope (FE-SEM, FEI Sirion) with an Energy-dispersive X-ray spectrometer (EDS) and transmission electron microscopy (JEOL-JEM2100F).

2.3. Electrochemical characterizations

Electrochemical performance was tested using CR2032 coin-type cells fabricated in air. The electrodes were prepared by mixing active material, conductive carbon and polyvinylidene fluoride (PVDF) in a mass ratio of 7: 2: 1 using N-methyl-2-pyrrolidone (NMP) as the solvent. Then the slurry was painted on the current collector (titanium foil) and heated at 120 °C in vacuum to remove NMP. The mass loadings of the working electrodes are about 2 mg cm^{-2} 3 M zinc trifluoromethanesulfonate (98%, $Zn(CF_3SO_3)_2$) aqueous solution was used as the electrolyte. Zinc metal and glass fiber filter (Whatman, Grade GF/A) was served as the anode and the separator.

Cyclic voltammetry (CV) in a voltage window of 0.2–1.6 V and electrochemical impedance spectroscopy (EIS) measurements in the frequency range from 100 kHz to 0.01 Hz were performed on a Solartron electrochemical station (SI 1287) with an electrochemical impedance spectroscopy system (EIS, SI 1260). The ion diffusion coefficient of the electrode material was calculated from the low frequency region of EIS plots based on the following equation:

$$D_{Zn^{2+}}^{EIS} = \frac{R^2T^2}{2A^2n^4F^4C^2\sigma_w^2} \quad (1)$$

where F, R and T represent the Faraday constant (96,500 C mol^{-1}), gas constant (8.314 J mol^{-1} K^{-1}) and absolute temperature (298 K), respectively. A, n and C are the surface area of the electrode (0.785 cm^2), number of electrons transferred per molecule (4) and concentration of ion (3*10^{-3} mol cm^{-3}) in the electrolyte. σ_w is the Warburg coefficient, which is the slope of the fit line for Z′ and angular frequency $\omega^{-1/2}$. Galvanostatic charge-discharge (GCD) were conducted using a Neware tester (CT-4008). The energy density E (Wh·kg^{-1}) and power density P (W·kg^{-1}) were calculated as follows:

$$E = \int_0^{\Delta t} IV(t)dt \quad (2)$$

$$P = E/t \quad (3)$$

where I is the current density (A·kg^{-1}) at different voltage V (V) and t is the discharge time (h).

3. Results and discussion

3.1. Composition and morphology of Al–VOH

Al–VOH and VOH were both synthesized through a one-step hydrothermal process. The obtained XRD pattern of VOH is well-indexed as $V_2O_5{\cdot}1.6H_2O$ (JCPDS, No. 40–1296) with an interlayer spacing of 11.8 Å calculated through the (001) peak at 7.4° based on the Bragg equation (Fig. 1a). The XRD pattern of Al–VOH is similar to JCPDS, No. 47–0146, $MnV_{12}O_{31}{\cdot}10H_2O$ (Fig. S1) [45], though the detailed structure information of this compound is unavailable. However, the XRD pattern of Al–VOH is similar to that of $M_xV_2O_5A_y{\cdot}nH_2O$ (M: cation; A: anion), $M_xV_2O_{5+y}{\cdot}nH_2O$ and $H_{0.4}V_2O_{5.2-\delta}{\cdot}nH_2O$ reported in literatures [37,46–48]. Among these formulas, $M_xV_2O_5A_y{\cdot}nH_2O$ can be excluded as no sulfur is tested in XPS and EDS [47]. We hypothesize the Al–VOH has a similar crystal structure with $M_xV_2O_{5+y}{\cdot}nH_2O$ as Al stably exists in the structure, which is consistent with the formula $MnV_{12}O_{31}{\cdot}10H_2O$. In this structure, the layered composition is the same as that of $H_{0.4}V_2O_{5.2-\delta}{\cdot}nH_2O$ ($0.04 < \delta < 0.2$), which consists of double layered [VO_6] octahedron and [VO_5] pyramid, while the interlayer space is occupied by water molecules and metal cations instead of protons (inset Fig. 1c) [46]. The peak at 6.6° indicates an enlarged interlayer spacing of 13.4 Å compared with that of VOH, further verifying the proposed structure in which Al^{3+} and water are introduced into the interlayer spacing. It is worth noting that this interlayer spacing is also larger than the reported MnVO with similar structure (12.9 Å) [37]. In consideration of the similar ionic radius of Al^{3+} (53.5 p.m.) and Mn^{2+} (58 p.m.), the enlarged interlayer spacing may be attributed to the stronger electrostatic repulsion between the layered V^{5+} and the higher valence Al (+3) compared to Mn (+2).

In Raman spectra, Al–VOH shows a spectrum similar to V_2O_5 (Fig. 1b). Peaks at 142 cm^{-1} are assigned to the bending vibration of -O-V-O- chains. A stronger relative intensity and a shift of 2 cm^{-1} to higher wavenumber of Al–VOH are observed compared with VOH (Fig. S2), indicating the cohesion of the layers is strengthened by the addition of Al^{3+} [49,50]. The bending and stretching vibrations of V^{5+}=O are located at 283 and 993 cm^{-1}, respectively [51,52]. The peak at 520 cm^{-1} is attributed to the stretching vibration of the vanadium and chain oxygen V–O and peaks at 408 and 700 cm^{-1} stem from the bending and stretching vibrations of vanadium and bridging oxygen V–O–V [53]. Lorentzians were employed to fit the peaks around 700 cm^{-1}. Besides the fitted peaks at about 670 and 700 cm^{-1} which correspond to the V–O stretching vibrations, another weak peak at 645 cm^{-1} appears in the fitting result of Al–VOH, which can be related to an Al–O bond, revealing strong chemical bonds instead of weak interactions were formed between Al and O atoms [54]. The peak at 1402 cm^{-1} in the FTIR spectrum of Al–VOH (Fig. 1c) also confirms the existence of Al–O bonds [55]. Other peaks are similar to those found in the FTIR spectrum of $V_2O_5{\cdot}nH_2O$, in which peaks at 1002, 759 and 515 cm^{-1} are attributed to

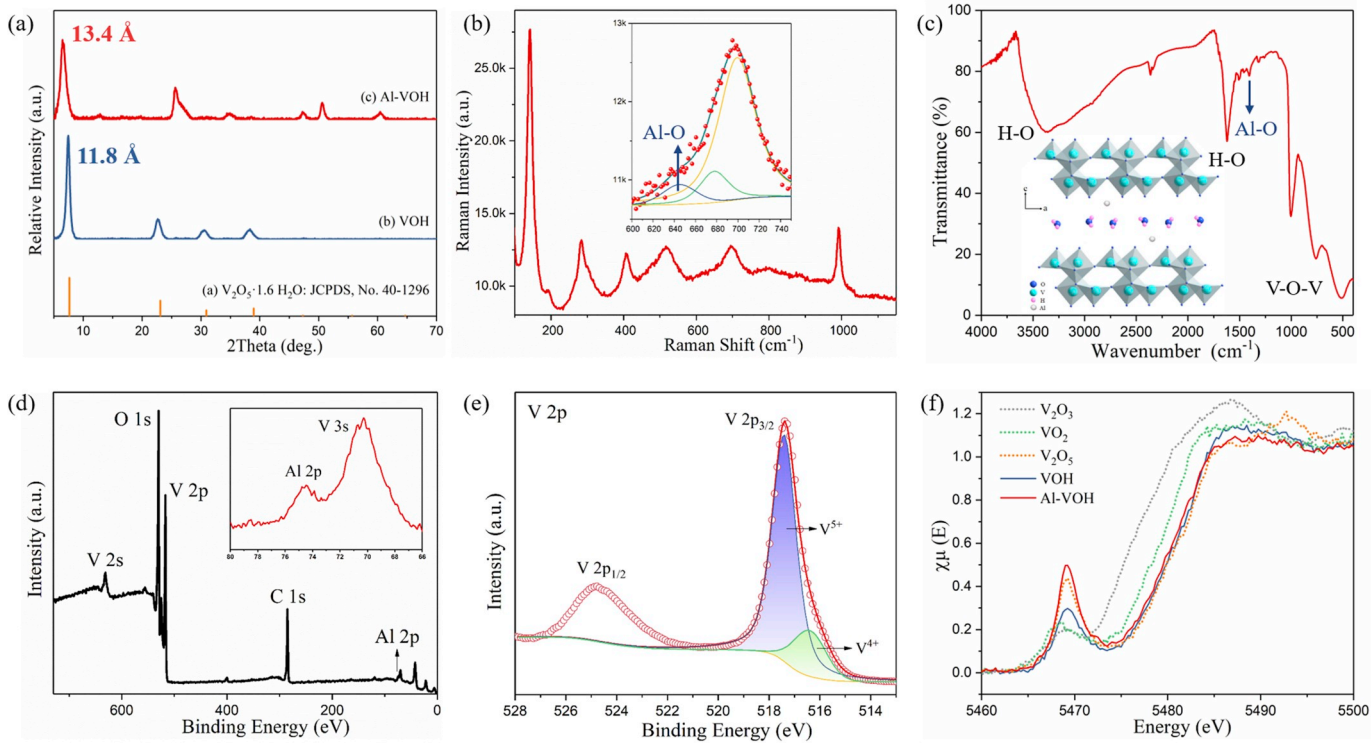

Fig. 1. (a) XRD patterns of Al–VOH and VOH. (b) Raman spectrum of Al–VOH, inset is the partially fitted spectra from 600 to 760 cm^{-1}. Al–O bond at 645 cm^{-1} suggests the existence of Al–O bond. (c) FTIR spectrum of Al–VOH, inset is the schematic of the possible crystal structure of Al–VOH. The XPS spectra of Al–VOH: (d) the survey scan spectrum and (e) high resolution spectrum of V 2p. (f) Normalized V K-edge XANES spectra of Al–VOH, VOH and standard V-based oxides with different valence states.

the symmetric stretching vibrations of V=O, and the asymmetric and symmetric stretching vibrations of V–O–V, respectively [56,57]. The broad peak at 3356 cm^{-1} and the peak at 1620 cm^{-1} verify the presence of interlayer water molecules. To maintain the electroneutrality of the compound, part of V^{5+} is reduced to V^{4+} during the introduction of Al^{3+}, which is proved by XPS results. By surveying the XPS spectrum of Al–VOH, V, O and Al elements can be identified (Fig. 1d). No signal of sulfur is detected, indicating the sulfate radical from the Al source is not involved in the reaction. The two fitted peaks at 516.4 eV and 517.4 eV are attributed to the V $2p_{3/2}$ electrons of V^{4+} and V^{5+}, respectively [58,59], and their ratio can be calculated by the integration areas of the fitted peaks. As displayed in Fig. 1e and Fig. S3, the V^{4+} ratio of 23.0% in Al–VOH is higher than that of VOH (12.3%) because of the addition of positive Al^{3+}. The peak of Al 2p located at 74.4 eV only occurs in the spectrum of Al–VOH (inset Fig. 1d), suggesting the successful introduction of Al^{3+} into VOH. The normalized V K-edge XANES measurements of Al–VOH and VOH were performed to analyze the molecular structure and oxidation state of V atoms in the bulk of the material, as shown in Fig. 1f [42]. Peaks presenting in the pre-edge region (~5469 eV) are important for elucidating the molecular symmetry of the metal center [42,44], and the intensities are also affected by the amount of unoccupied d orbitals. Of the empirical standards chosen here, both V_2O_3 and VO_2 consist of symmetric [VO_6] octahedron, but V^{3+} has fewer unoccupied d orbitals, leading to a slightly lower intensity. While V^{5+} has more unoccupied d orbitals, it exhibits the largest pre-edge intensity because the V_2O_5 crystal consists of asymmetric [VO_5] pyramids. For VOH, the intensity of the pre-edge peak is between those of VO_2 and V_2O_5, confirming the proposed structure inset Fig. 1c with alternant [VO_6] octahedron and [VO_5] pyramid. However, the peak of Al–VOH is much higher than that of VOH. As the proportion of V^{4+} is higher, the larger intensity is because of the increased crystal asymmetry caused by the introduction of Al^{3+}, which results in a further distortion due to the Al–O coordination and oxygen vacancies [60–62]. The proportions of V^{4+} in bulk Al–VOH and VOH calculated from the V K-edge position are 29.3% and 13.0%, respectively [63]. As the ratio of Al:V measured by ICP is 0.07:1, the increased proportion of V^{4+} should be 21% considering the electroneutrality. The actual increase in V^{4+} upon incorporation of Al is 16.3%, suggesting a quantity of O atoms were also introduced into the structure concurrently with Al^{3+}, thus the roughly inferred formula is $Al_{0.84}V_{12}O_{30.3}{\cdot}nH_2O$, which is also in consistent with the $M_xV_2O_{5+y}{\cdot}nH_2O$.

Al–VOH consists of microspheres with diameters in the range of 5–20 μm, as shown in SEM images (Fig. 2a and b). The magnified image reveals that the microspheres are composed of nanosheets. TEM images of Al–VOH (Fig. 2c–e) also confirm the aggregation of nanosheets. The HRTEM image shown in Fig. 2e indicates a polycrystalline structure, and the observed interfringe spacings of 0.18, 0.19, and 0.23 nm are in accordance with the peaks at 50.6, 48.9 and 38.6° in the XRD pattern, respectively. VOH also exhibits a polycrystalline layered structure with an interfringe spacing of 0.20 nm (Fig. S4), which is corresponding to the (006) plane. EDS mappings of Al–VOH collected by TEM shown in Fig. 2f reveal the homogeneous distribution of V, O, and Al elements. The atomic ratio of Al:V is estimated to be about 0.09:1, which is close to the ICP result (0.07:1) but much lower than the ratio of raw materials, indicating possibly only a fraction of added Al^{3+} enters the Al–VOH crystal structure.

3.2. Electrochemical properties of Al–VOH

Cyclic voltammetry (CV) curves were collected at 0.1 mV s^{-1} in the voltage range of 0.2–1.6 V for three cycles. The third cycle of Al–VOH and VOH CV curves are compared in Fig. 3a, both of which have two main pairs of redox peaks at around 1.0 and 0.5 V, corresponding to the redox pairs V^{5+}/V^{4+} and V^{4+}/V^{3+}, respectively. Compared with VOH, Al–VOH shows smaller voltage gaps and higher peak currents on both pairs of redox peaks (summarized in Table 1), suggesting a smaller polarization due to the faster ion diffusion and better redox reaction kinetics, which will be detailed discussed below. Compared with VOH, the center positions of V^{5+}/V^{4+} and V^{4+}/V^{3+} redox couples in Al–VOH also shift from 1 to 0.96 V and 0.54–0.58 V respectively, suggesting the introduced Al^{3+} not only facilitates the redox reaction kinetically, but also thermodynamically changes the Gibbs free energy of the products. The first CV curves of Al–VOH and VOH are incomplete (Fig. S5) because the tests were set to begin from the natural open current voltage, and the

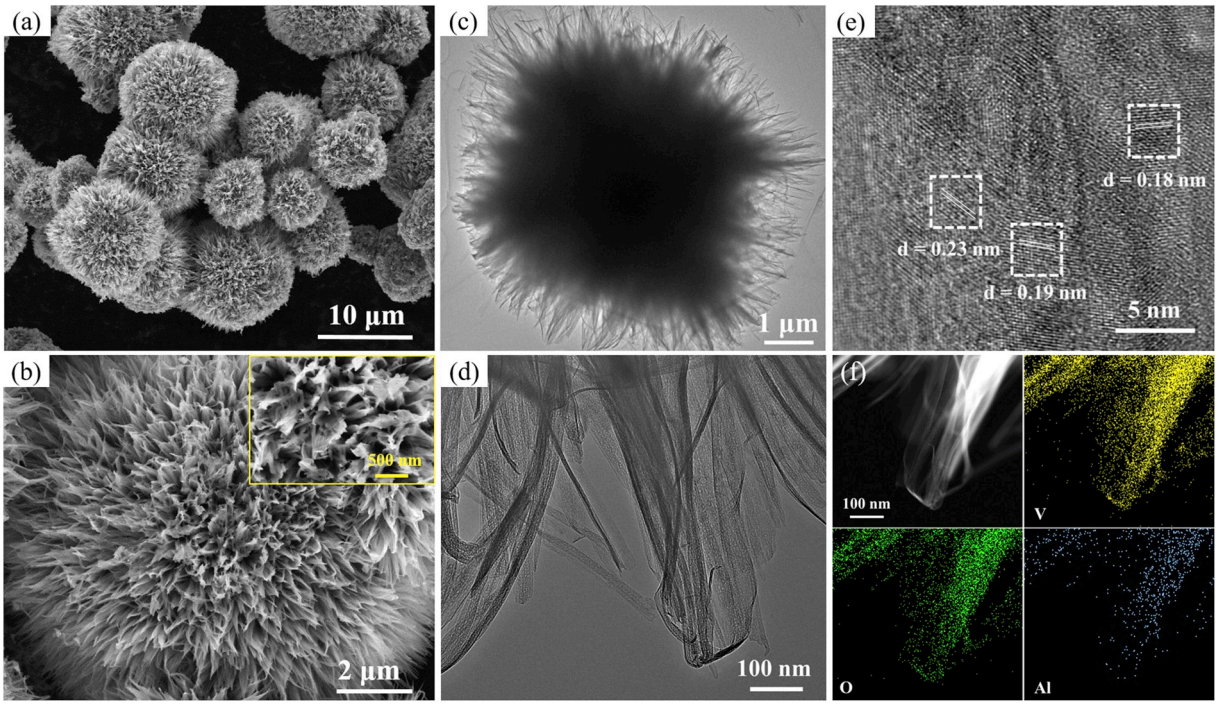

Fig. 2. SEM images (a–b), TEM images (c–d), the HRTEM image (e) and EDS mapping (f) of Al–VOH. Al–VOH shows a morphology of urchin-like microspheres consisting of nanosheets, and all elements have homogeneous distributions.

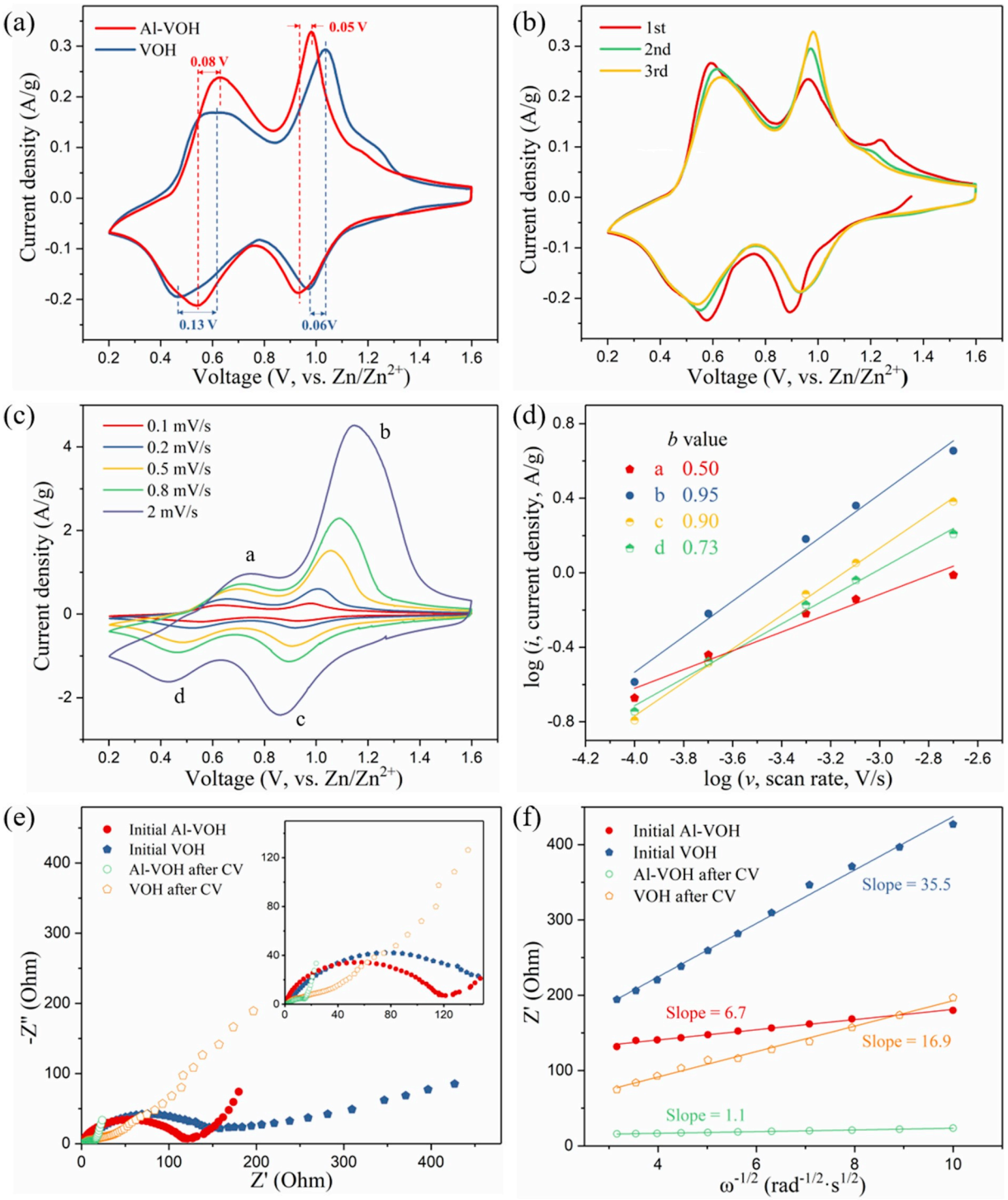

Fig. 3. (a) Comparison of the third cycle CV curves of Al–VOH and VOH at 0.1 mV s^{-1}. (b) Initial three CV curves of Al–VOH collected at 0.1 mV s^{-1}. (c) CV curves of Al–VOH collected at different scan rates and (d) log (*i*) vs. log (*v*) plots of four peaks in the CV curves. (e) Nyquist plots of Al–VOH and VOH before and after CV tests in the frequency range from 100 kHz to 0.01 Hz and (f) the corresponding relationship between frequency and real resistance in the low frequency region.

fully charged voltage (1.6 V) was considered as the end of each cycle for better comparison. The different open current voltages also indicate the thermodynamic effect of Al^{3+}. Small peaks at about 1.2 V observed in both materials, which were also reported in other similar materials fade away in the subsequent cycles, suggesting they are caused by the irreversible side reaction [37,40]. The gap of redox pairs V^{4+}/V^{3+} for Al–VOH (0.018 V) is much smaller than that of VOH (0.17 V) in the first cycle, which can be attributed to the fast ion diffusion resulted from the enlarged interlayer space. While the gap in the CV curves of VOH decreases in the third cycle compared with the first one, which is reasonable because the electrode activation can reduce the polarization. Nonetheless, in Al–VOH, the gap increases to 0.08 V in the third cycle. The similar shapes in the first three cycles of Al–VOH indicate a reversible redox process (Fig. 3b), but the reduction peak of V^{5+}/V^{4+} shows an obvious shift of 0.04 V to a higher voltage after the first cycle, while V^{4+}/V^{3+} reduction peak shifts 0.03 V to a lower voltage in the third cycle, leading to the increased gap compared with the first cycle. A probable hypothesis is the incomplete de-intercalation of Zn-ions in the

Table 1
Comparison of the peaks positions and voltage gaps in Al–VOH and VOH at.1 mV s^{-1}.

Sample		Peak position (V)	Voltage gap (V)	Center position (V)
Al–VOH	V^{5+}/V^{4+}	0.98/0.93	0.05	0.955
	V^{4+}/V^{3+}	0.62/0.54	0.08	0.580
VOH	V^{5+}/V^{4+}	1.03/0.97	0.06	1.000
	V^{4+}/V^{3+}	0.61/0.48	0.13	0.545

first cycle. A slight amount of Zn^{2+} were trapped resulting in a higher proportion of low-valence V as well as less obvious lattice contraction, thus facilitating the subsequent intercalation of Zn^{2+} during reduction of V^{5+} [64]. However, this also generates a higher total amount of Zn^{2+} occupied in the crystal lattice, leading to less channels but stronger electrostatic interaction for further ion diffusion, and eventually making a higher degree of electrode polarization in the subsequent reduction of V^{4+}.

CV curves at various scan rates were measured to further investigate the electrochemical kinetics. The voltage gaps of redox peaks increase with the increasing scan rate due to polarization (Fig. 3c and Fig. S6a) [37]. The following empirical equation of the peak current *i* and the scan rate *v* is employed to analyze the dominant factor governing the electrochemical process [65,66]:

$$i = av^b \quad (4)$$

in which parameter *a* and *b* are adjustable. For Al–VOH, The calculated *b* values of the oxidation peaks and reduction peaks of V^{5+}/V^{4+} are 0.95 and 0.90 respectively (Fig. 3d), which are higher than that of VOH (0.85 and 0.80, Fig. S6b), indicating the improved ion diffusion rate and predominant non-diffusion controlled process in this reaction. Lower *b* values of V^{4+}/V^{3+} peaks (0.50/0.73) are calculated compared to VOH (0.66/0.76), revealing the process is mostly diffusion controlled. Nevertheless, higher current densities of the redox peaks and a smaller voltage gap between V^{4+}/V^{3+} peaks are still observed in Fig. 3a, indicating a faster ion diffusion rate of Al–VOH in this process compared with that of VOH. The reduced *b* values could attribute to a faster redox reaction facilitated by the increased concentration of Zn^{2+} and the introduction of Al^{3+}, resulting in a relatively diffusion-controlled process. The current at a fixed voltage of a certain scan rate (v) can be divided into capacitive (k_1v) and diffusion-controlled ($k_2v^{1/2}$) contributions based on the equation:

$$i = k_1v + k_2v^{1/2} \quad (5)$$

where coefficients k_1 and k_2 can be quantitatively calculated through the fitting of $i/v^{1/2}$ *vs.* $v^{1/2}$ plots according to the variant of Equation (5):

$$i/v^{1/2} = k_1v^{1/2} + k_2 \quad (6)$$

In Al–VOH, a 33.5% fraction of the capacity is assigned to the capacitive contribution at a scan rate of 0.1 mV s^{-1}, and the capacitive contribution gradually increases to 67.3% at a scan rate of 2 mV s^{-1}, as shown in Fig. S7. It is noteworthy that the capacitive contribution is high for V^{5+}/V^{4+} peaks while much lower for V^{4+}/V^{3+} peaks, which is in accordance with the results of *b* values.

The increased ion diffusion rate of Al–VOH can be proved by the high slope at the low frequency region in the Nyquist plot (Fig. 3e), and the calculated ion diffusion coefficients based on the slope of Z'-$\omega^{-1/2}$ (Fig. 3f) of Al–VOH and VOH are 5.6×10^{-13} and 2.0×10^{-14} cm^2 s^{-1}. The significant acceleration of the Zn^{2+} migration can be mainly attributed to the expanded interlayer spacing. The diffusion coefficient of Al–VOH is also one order of magnitude higher than that reported for MnVO (6.07×10^{-14} cm^2 s^{-1}) [37], which has similar structure but smaller interlayer spacing, implying the interlayer spacing could be the key factor governing the ion migration. The regular nanosheets of Al–VOH can also provide sufficient contact area between the active material and electrolyte, thus shorten the pathways and enhance the ion diffusion coefficient. The charge transfer resistance (R_{ct}) represented by the semicircle in the high frequency region of Al–VOH is about 118 Ω, which is lower than the 147 Ω of VOH, suggesting an enhanced electron transfer rate [67]. The main reason is the increased proportion of V^{4+} in Al–VOH provides more d-electrons, which can improve the conductivity. Oxygen vacancies can also narrow the band gap [68,69] and promote the electron transfer. Besides, the layers are connected by Al–O bonds in Al–VOH, providing access for highly efficient electron transfer. After 15 times of CV cycles, the diffusion coefficients of Al–VOH and VOH are raised to 2.1×10^{-11} and 8.7×10^{-14} cm^2 s^{-1} respectively, along with reduced R_{ct}. This phenomenon may be due to the improved wettability of the electrodes and the electro-activation process caused by the trapped Zn^{2+}, and can also explain rising capacities at the beginning of the cycling process.

The above discussion supports the hypothesis that the ion and electron transfer is enhanced in Al–VOH, which leads to a high capacity of 380 mAh·g^{-1} at 50 mA g^{-1}, as shown in Fig. 4a. Although having a larger interlayer spacing and a higher diffusion coefficient, the capacitance of Al–VOH is slightly lower than that of MnVO, which might be due to the higher percentage of V^{4+} in Al–VOH (23.0% by XPS) than that in MnVO (19% by XPS), causing a reduced ability for electron storage. Nonetheless, the capacity of Al–VOH is still higher or comparable with other reported vanadium-based materials, as listed in Table S1. The discharge capacities of Al–VOH at current densities of 0.5, 1, 2, 4 and 8 A g^{-1} are 329, 308, 283, 245 and 195 mAh·g^{-1}, respectively, which are higher than VOH (274 mA g^{-1} at 0.5 A g^{-1}, Fig. 4b). The capacity of Al–VOH is stable at a high current density of 8 A g^{-1} and can recover to the initial value when the rate returns, verifying the great electrochemical reversibility and crystal structure stability of Al–VOH at high rates. The cycling stability of Al–VOH at low rates is less ideal (Fig. S8), which is in a good agreement with literature data [26,70–72]. One possible explanation is that the slow and deep insertion of Zn^{2+} into the crystal lattice at low currents leads to a high initial capacity but severe degradation of the layered crystal structure [72,73]. The improved structure stability of Al–VOH was further proved by the excellent long-term cycling performance (Fig. 4c). At a current density of 4 A g^{-1}, the Al–VOH delivers an initial capacity of 221 mAh·g^{-1}, then the capacity gradually increases to 260 mAh·g^{-1} (117% of the initial capacity) during the first 200 cycles because of the electro-activation process resulted from a combination of reasons. Firstly, the fully infiltrated of the electrolyte leads to an improved utilization of the active material [74]. More importantly, the trapped Zn^{2+} can connect the [VO_n] interlayers to provide more charge transfer pathways and lead to a lower resistance, which can be confirmed by the much smaller R_{ct} after the CV cycles (about 14 Ω) compared with the initial R_{ct} [37]. Besides, as mentioned above, the ion diffusion coefficient of Al–VOH is increased by two orders of magnitude after activation, which is more significant compared with the 4 times increase of VOH. The large difference can be attributed to the enhanced structural stability of Al–VOH caused by the introduction of Al^{3+} along with the trapped Zn^{2+}. While for VOH, the structure degradation of the intrinsically unstable layered structure with less trapped Zn^{2+} results in relatively insignificant enhancement of diffusion coefficient and a fast capacity decrease during cycling. Only a slight decline is observed in the following cycles of Al–VOH, and the capacity is still 107% of the initial value after 3000 cycles. The SEM image (Fig. S9) indicates the initial morphology of Al–VOH is well maintained after cycling, and the atomic ratio of Al:V is estimated to be about 0.066:1 by the EDS spectrum (Fig. S10), revealing little Al^{3+} deintercalation during the cycling because of the stable Al–O bond. While the capacity of VOH suffers a rapid decline to only 38% of its initial capacity after 3000 cycles, suggesting a greatly enhanced stability of the crystal structure by introducing Al^{3+}. Such good performance of

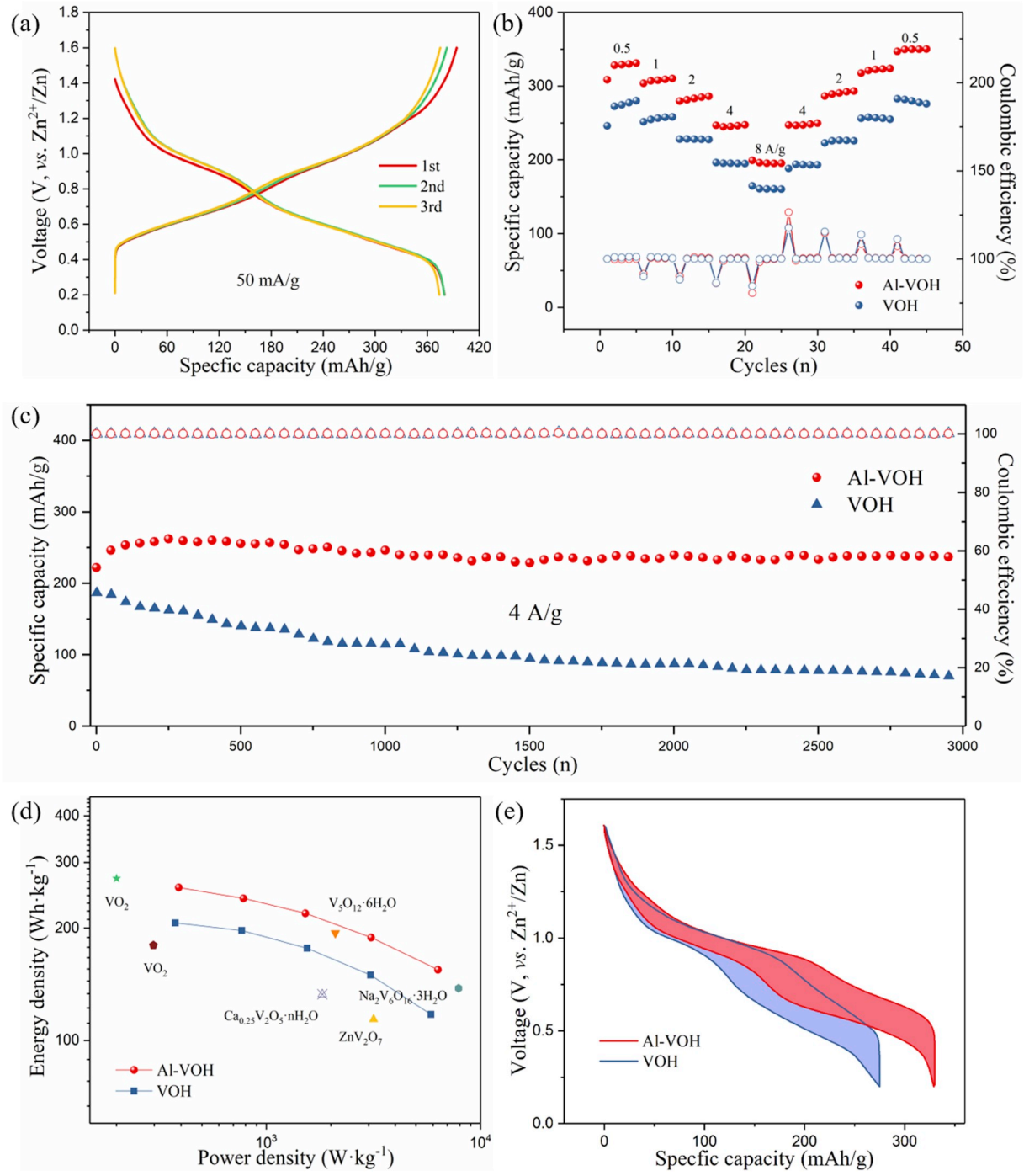

Fig. 4. (a) GCD curves of Al–VOH at 50 mA g^{-1}. (b) Comparison of the rate capability and (c) cycling stability of Al–VOH and VOH. (d) Ragone plots of the Zn-ion batteries using different cathodes, including $Ca_{0.25}V_2O_5{\cdot}nH_2O$ [24], $Na_2V_6O_{16}{\cdot}3H_2O$ [35], $V_5O_{12}{\cdot}6H_2O$ [75], VO_2 [76,77], ZnV_2O_7 [79]. (e) Comparison of the GCD curves of Al–VOH and VOH at 0.5 A g^{-1}.

Al–VOH is competitive with some other reported V-based cathode materials, as listed in Table S1. Ragone plots of Al–VOH and VOH batteries calculated from discharge curves of current densities from 0.5 to 8 A g^{-1} are shown in Fig. 4d. Al–VOH exhibits an energy density of 257 Wh·kg^{-1} at a power density of 390 W kg^{-1}, and the maximum power density can reach 6.3 kW kg^{-1}, which are better than those of VOH and some other V-based cathodes, such as $Ca_{0.25}V_2O_5{\cdot}nH_2O$ [24], $V_5O_{12}{\cdot}6H_2O$ [75], and VO_2, [76,77]. More importantly, compared with VOH, Al–VOH shows higher energy efficiencies, which are defined as the ratio of discharge and charge energy densities [78]. The encircled area by the charge-discharge curves indicates the energy loss, as exhibited in Fig. 4e and Fig. S11. The energy efficiencies of Al–VOH at 0.5 and 4 A g^{-1} are 83% and 69%, which are higher than that of VOH (79% and 61%). The difference between energy efficiencies of Al–VOH and VOH is more obvious after 3000 cycles (59% and 30% respectively), which can attribute to fewer side reactions and a lower degree of polarization of Al–VOH, further confirming the introduction of Al^{3+} can effectively improve the electrochemical performance, especially the cycling stability of layered V-oxides.

Fig. 5a is the *ex-situ* XRD patterns of the Al–VOH electrodes for the first two cycles of the full discharge-charge process. After the first discharge, the slight expansion of the interlayer spacing can be

confirmed by the shift of the peaks to lower Bragg angles, which is more obvious for the peaks at higher angles. Peaks at 13.1° and 19.8° with *d*-spacings of 6.75 and 4.5 Å correspond to the (002) and (003) planes, with an interlayer spacing of 13.5 Å. These two peaks can be observed in the zoomed in XRD pattern of initial Al–VOH, as marked in Fig. S12. After discharged, the intercalated Zn^{2+} is likely to deteriorate the original highly ordered crystal structure and resulted in a significant decrease of the crystallinity, leading to a relatively increase of intensities of the peaks at higher angles. Besides, both peaks shift with the main (001) peak because of the variation of interlayer spacing caused by the intercalation-deintercalation of Zn^{2+} in the following patterns, confirming these peaks belong to the original phase instead of a new phase. The interlayer spacing of the electrode material decreases to 12.5 Å when fully charged, which is smaller than the initial spacing. This

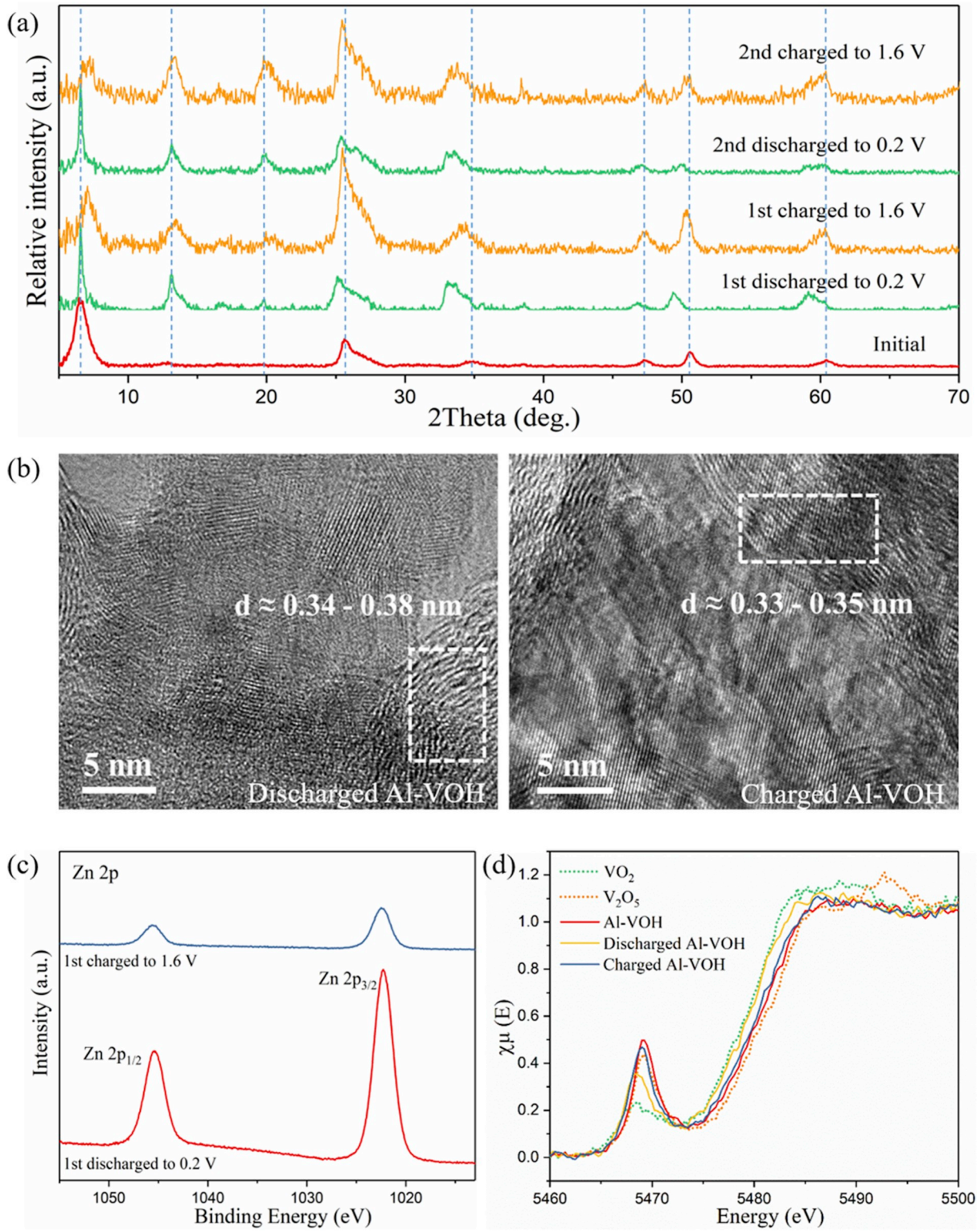

Fig. 5. (a) *Ex-situ* XRD patterns of the fully discharged and charged Al–VOH electrode materials. HRTEM images (b), high resolution XPS spectra of Zn 2p (c) and normalized V K-edge XANES spectra (d) of the first discharged and charged Al–VOH electrode materials.

phenomenon can be attributed to the de-intercalation of interlayer water along with the Zn^{2+} as proposed in the literature [10]. The disorder of the crystal structure may increase with the deintercalation of Zn^{2+}, leading to a relatively low intensity of the (001) plane. The patterns of the second cycle show similar trends with the first, indicating the electrochemical process is highly reversible. XRD patterns of the discharged and charged VOH electrodes are displayed in Fig. S13. The patterns are similar with that of Al–VOH, further confirming the hypothesized structure of Al–VOH, which has a similar layered structure to VOH but has cations occupying the interlayer space. The (001) peak of VOH divided into two peaks at 6.4° (13.7 Å) and 8.6° (10.3 Å) after the first charge, indicating the uneven intercalation of Zn^{2+} because of low ion migration rate. The lattice spacing decreased to 12.2 Å after charged, with a larger variation of 1.5 Å compared with Al–VOH (0.9 Å). The intense changes may accelerate the structural degradation and lead to the poor cycling stability of VOH. Further research on *in-situ* XRD patterns during the charge-discharge process is still needed to achieve detailed information of the structural evolution and analyze exact reaction occurred at each voltage segment.

HRTEM images of discharged and charged Al–VOH shown in Fig. 5b also demonstrate slight changes of the crystal structure. TEM-EDS (Figs. S14 and 15) and SEM-EDS are carried out to determine the Zn:V ratios of the electrode materials, and the results are summarized in Table S2. The Zn:V ratios of discharged/charged Al–VOH electrodes are found to be 1.5:1 and 0.6:1 by SEM-EDS, which are higher than that of VOH (0.4:1 and 0.25:1). The reason the Zn content is higher than the theoretical value might be because EDS is a surface test, and the results are affected by the electrolyte residue and the atomic number of the element. Though the data are not absolutely precise, the trend is clear. Compared with VOH, larger amount of Zn^{2+} intercalates into Al–VOH due to its excellent ion diffusion coefficient and conductivity. Although the de-intercalated Zn^{2+} content is also higher, which corresponds with its better capacity, there is still a higher proportion of trapped Zn^{2+} in Al–VOH when fully charged. High resolution Zn 2p XPS spectra of discharged/charged electrode materials shown in Fig. 5c also demonstrate the existence of trapped Zn^{2+} in the fully charged Al–VOH. In XANES spectra (Fig. 5d), the pre-edge peak intensity of the discharged Al–VOH decreased on account of the lower proportion of unoccupied d orbital caused by the reduction of V. When charged, the peak is still slight lower in intensity than the initial Al–VOH. This trend is also in good agreement with the calculated proportions of V^{4+} in the discharged and charged Al–VOH based on the shift of K-edge, which are 87.0% and 45.4% respectively, confirming the existence of trapped Zn^{2+}, as well as the increased proportion of V^{4+} after the first charge. It is worth noting that the weight contents of Al in discharged/charged electrode materials determined by ICP are 0.80% and 0.67%, indicating little Al^{3+} de-intercalation during the charge process due to the strong chemical bond connection. These results confirm the above discussion of the CV results. The trapped Zn^{2+} can yield a higher proportion of V^{4+}, which can facilitate the subsequent electrochemical process. The higher concentration of Zn^{2+} also accelerates the redox reaction during the V^{4+}/V^{3+} process. On the other hand, a higher proportion of trapped Zn^{2+} in Al–VOH can also serve as pillars along with Al-ions, helping to avoid severe lattice contraction and the degradation of the layered structure during cycling, thus leading to a greatly enhanced stability.

4. Conclusions

The Al–VOH possesses expanded lattice spacing and improved diffusivity and electrical conductivity as well as an increased proportion of V^{4+} cations, resulting in the enhanced rate of ion diffusion and electron transfer. It is noted that the incorporation of trivalent aluminum ions resulted in the greatest increase of the interplanar spacing, even though Al^{3+} has the smallest ionic radius as compared with both mono and divalent metal cations, indicating the ionic radius is not the only factor determining the interplanar spacing. Al–VOH delivers a high capacity of 380 mAh·g^{-1} at 50 mA g^{-1} as a cathode material for ZIBs, as well as excellent rate capability (245 mAh·g^{-1} at 4 A g^{-1}) and cycling stability (no decline after 3000 cycles). It is possible that only a small fraction of Al-ions entered the crystal structure, but appreciably improved the structural stability along with trapped Zn^{2+} after the first charge process, which prevent the degradation of the structure and facilitate the highly reversible electrochemical reaction. It is possible the Zn-ion intercalation capacity may be further enhanced if more trivalent aluminum ions are successfully incorporated into VOH. The variation of interplanar space when incorporated with different sized cations may also help to find a way to minimize the volume expansion and contraction of active materials when subjected to ion insertion and extraction; more work along this direction in our lab is under way.

Declaration of competing interest

There are no conflicts of interest to declare.

Acknowledgements

This work was supported by the National Science Foundation (CBET-1803256). Part of this work was conducted at the Molecular Analysis Facility, a National Nanotechnology Coordinated Infrastructure site at the University of Washington which is supported in part by the National Science Foundation (grant NNCI-1542101), the University of Washington, the Molecular Engineering & Sciences Institute, and the Clean Energy Institute. This work was also partially supported by the National Natural Science Foundation of China (Grant No. 21601026, 21771030). J. Zheng and M. Tian acknowledges the financial support from China Scholarship Council (No. 201806060032, 201806740050). E. Jahrman was supported by a subcontract from the National Institute of Standards and Technology. Opinions, recommendations, findings, and conclusions presented in this manuscript and associated materials do not necessarily reflect the views or policies of NIST or the United States Government.

Appendix A. Supplementary data

Supplementary data to this article can be found online at https://doi.org/10.1016/j.nanoen.2020.104519.

References

[1] D. Larcher, J.M. Tarascon, Nat. Chem. 7 (2014) 19.
[2] D. Chen, X.H. Rui, Q. Zhang, H.B. Geng, L.Y. Gan, W. Zhang, C.C. Li, S.M. Huang, Y. Yu, Nano Energy 60 (2019) 171–178.
[3] P. Saha, M.K. Datta, O.I. Velikokhatnyi, A. Manivannan, D. Alman, P.N. Kumta, Prog. Mater. Sci. 66 (2014) 1–86.
[4] X. Lu, M. Yu, G. Wang, Y. Tong, Y. Li, Energy Environ. Sci. 7 (2014) 2160–2181.
[5] B. Dunn, H. Kamath, J.-M. Tarascon, Science 334 (2011) 928–935.
[6] M. Li, J. Lu, Z. Chen, K. Amine, Adv. Mater. 30 (2018) 1800561.
[7] B. Tang, L. Shan, S. Liang, J. Zhou, Energy Environ. Sci. 12 (2019) 3288–3304.
[8] L. Dong, X. Ma, Y. Li, L. Zhao, W. Liu, J. Cheng, C. Xu, B. Li, Q.-H. Yang, F. Kang, Energy Storage Mater. 13 (2018) 96–102.
[9] H. Kim, J. Hong, K.-Y. Park, H. Kim, S.-W. Kim, K. Kang, Chem. Rev. 114 (2014) 11788–11827.
[10] C. Xia, J. Guo, P. Li, X.X. Zhang, H.N. Alshareef, Angew. Chem. Int. Ed. 57 (2018) 3943–3948.
[11] X. Dai, F. Wan, L. Zhang, H. Cao, Z. Niu, Energy Storage Mater. 17 (2019) 143–150.
[12] H.D. Yoo, I. Shterenberg, Y. Gofer, G. Gershinsky, N. Pour, D. Aurbach, Energy Environ. Sci. 6 (2013) 2265–2279.
[13] J. Shin, D.S. Choi, H.J. Lee, Y. Jung, J.W. Choi, Adv. Energy Mater. 9 (2019) 1900083.
[14] P. Yu, Y. Zeng, H. Zhang, M. Yu, Y. Tong, X. Lu, Small 15 (2019).
[15] J.F. Parker, J.S. Ko, D.R. Rolison, J.W. Long, Joule 2 (2018) 2519–2527.
[16] A. Konarov, N. Voronina, J.H. Jo, Z. Bakenov, Y.-K. Sun, S.-T. Myung, ACS Energy Lett. 3 (2018) 2620–2640.
[17] Y. Li, J. Fu, C. Zhong, T. Wu, Z. Chen, W. Hu, K. Amine, J. Lu, Adv. Energy Mater. 9 (2019) 1802605.
[18] G.Z. Fang, J. Zhou, A.Q. Pan, S.Q. Liang, ACS Energy Lett. 3 (2018) 2480–2501.
[19] J. Ming, J. Guo, C. Xia, W.X. Wang, H.N. Alshareef, Mater. Sci. Eng. R 135 (2019) 58–84.
[20] M. Song, H. Tan, D.L. Chao, H.J. Fan, Adv. Funct. Mater. 28 (2018) 1802564.

[21] X.H. Zeng, J.N. Hao, Z.J. Wang, J.F. Mao, Z.P. Guo, Energy Storage Mater. 20 (2019) 410–437.
[22] D. Selvakumaran, A. Pan, S. Liang, G. Cao, J. Mater. Chem. 7 (2019) 18209–18236.
[23] P. Liu, K. Zhu, Y. Gao, H. Luo, L. Lu, Adv. Energy Mater. 7 (2017) 1700547.
[24] N. Zhang, F.Y. Cheng, Y.C. Liu, Q. Zhao, K.X. Lei, C.C. Chen, X.S. Liu, J. Chen, J. Am. Chem. Soc. 138 (2016) 12894–12901.
[25] Y. Zhang, H. Jiang, L. Xu, Z. Gao, C. Meng, ACS Appl. Energy Mater. 2 (2019) 7861–7869.
[26] Y. Yang, Y. Tang, G. Fang, L. Shan, J. Guo, W. Zhang, C. Wang, L. Wang, J. Zhou, S. Liang, Energy Environ. Sci. 11 (2018) 3157–3162.
[27] F. Liu, Z.X. Chen, G.Z. Fang, Z.Q. Wang, Y.S. Cai, B.Y. Tang, J. Zhou, S.Q. Liang, Nano-Micro Lett. 11 (2019) 25.
[28] M. Yu, Y. Zeng, Y. Han, X. Cheng, W. Zhao, C. Liang, Y. Tong, H. Tang, X. Lu, Adv. Funct. Mater. 25 (2015) 3534–3540.
[29] M.Y. Yan, P. He, Y. Chen, S.Y. Wang, Q.L. Wei, K.N. Zhao, X. Xu, Q.Y. An, Y. Shuang, Y.Y. Shao, K.T. Mueller, L.Q. Mai, J. Liu, J.H. Yang, Adv. Mater. 30 (2018) 6.
[30] N. Zhang, Y. Dong, M. Jia, X. Bian, Y.Y. Wang, M.D. Qiu, J.Z. Xu, Y.C. Liu, L.F. Jiao, F.Y. Cheng, ACS Energy Lett. 3 (2018) 1366–1372.
[31] S. Guo, G. Fang, S. Liang, M. Chen, X. Wu, J. Zhou, Acta Mater. 180 (2019) 51–59.
[32] D. Kundu, B.D. Adams, V. Duffort, S.H. Vajargah, L.F. Nazar, Nat. Energy 1 (2016) 16119.
[33] F. Wan, L. Zhang, X. Dai, X. Wang, Z. Niu, J. Chen, Nat. Commun. 9 (2018) 1656.
[34] F.W. Ming, H.F. Liang, Y.J. Lei, S. Kandambeth, M. Eddaoudi, H.N. Alshareef, ACS Energy Lett. 3 (2018) 2602–2609.
[35] V. Soundharrajan, B. Sambandam, S. Kim, M.H. Alfaruqi, D.Y. Putro, J. Jo, S. Kim, V. Mathew, Y.K. Sun, J. Kim, Nano Lett. 18 (2018) 2402–2410.
[36] P. Hu, T. Zhu, X. Wang, X. Wei, M. Yan, J. Li, W. Luo, W. Yang, W. Zhang, L. Zhou, Z. Zhou, L. Mai, Nano Lett. 18 (2018) 1758–1763.
[37] C. Liu, Z. Neale, J. Zheng, X. Jia, J. Huang, M. Yan, M. Tian, M. Wang, J. Yang, G. Cao, Energy Environ. Sci. 12 (2019) 2273–2285.
[38] N.N. Greenwood, A. Earnshaw, Chemistry of the Elements, second ed., Butterworth-Heinemann, Oxford, 1997.
[39] Y.-R. Luo, Comprehensive Handbook of Chemical Bond Energies, CRC Press, Boca Raton, 2007.
[40] l. Qian, T. Wei, K. Ma, G. Yang, C. Wang, ACS Appl. Mater. Interfaces 11 (2019) 20888–20894.
[41] W. Zhang, S. Liang, G. Fang, Y. Yang, J. Zhou, Nano-Micro Lett. 11 (2019) 69.
[42] G.T. Seidler, D.R. Mortensen, A.J. Remesnik, J.I. Pacold, N.A. Ball, N. Barry, M. Styczinski, O.R. Hoidn, Rev. Sci. Instrum. 85 (2014) 113906.
[43] W. Bi, E. Jahrman, G. Seidler, J. Wang, G. Gao, G. Wu, M. Atif, M. AlSalhi, G. Cao, ACS Appl. Mater. Interfaces 11 (2019) 16647–16655.
[44] E.P. Jahrman, W.M. Holden, A.S. Ditter, D.R. Mortensen, G.T. Seidler, T.T. Fister, S.A. Kozimor, L.F.J. Piper, J. Rana, N.C. Hyatt, M.C. Stennett, Rev. Sci. Instrum. 90 (2019), 024106.
[45] S. Zhang, M. Hou, L. Hou, W. Ma, Manganese Vanadate Nanomaterial: Synthesis and Application, China Pat., 2015.
[46] E. Potiron, A. Le Gal La Salle, A. Verbaere, Y. Piffard, D. Guyomard, Electrochim. Acta 45 (1999) 197–214.
[47] C.C. Torardi, C.R. Miao, M.E. Lewittes, Z. Li, J. Solid State Chem. 163 (2002) 93–99.
[48] E. Potiron, A. Le Gal La Salle, A. Verbaere, Y. Piffard, D. Guyomard, M. Tournoux, J. Phys. Chem. Solid. 62 (2001) 1447–1455.
[49] K. Zhu, H. Qiu, Y. Zhang, D. Zhang, G. Chen, Y. Wei, ChemSusChem 8 (2015) 1017–1025.
[50] S. Zhan, Y. Wei, X. Bie, C. Wang, F. Du, G. Chen, F. Hu, J. Alloys Compd. 502 (2010) 92–96.
[51] F.D. Hardcastle, I.E. Wachs, J. Phys. Chem. 95 (1991) 5031–5041.
[52] Z. Wu, P.C. Stair, S. Rugmini, S.D. Jackson, J. Phys. Chem. C 111 (2007) 16460–16469.
[53] R. Baddour-Hadjean, M.B. Smirnov, V.Y. Kazimirov, K.S. Smirnov, J.-P. Pereira-Ramos, J. Raman Spectrosc. 46 (2015) 406–412.
[54] A. Aminzadeh, H. Sarikhani-fard, Spectrochim. Acta Mol. Biomol. Spectrosc. 55 (1999) 1421–1425.
[55] Y. Xu, D. Sun, Chem. Eng. J. 183 (2012) 332–338.
[56] G.P. Holland, F. Huguenin, R.M. Torresi, D.A. Buttry, J. Electrochem. Soc. 150 (2003) A721–A725.
[57] J. Zheng, Y. Zhang, T. Hu, T. Lv, C. Meng, Cryst. Growth Des. 18 (2018) 5365–5376.
[58] H. Song, C. Liu, C. Zhang, G. Cao, Nano Energy 22 (2016) 1–10.
[59] J. Zheng, Y. Zhang, Q. Wang, H. Jiang, Y. Liu, T. Lv, C. Meng, Dalton Trans. 47 (2018) 452–464.
[60] G.A. Horrocks, E.J. Braham, Y. Liang, L.R. De Jesus, J. Jude, J.M. Velázquez, D. Prendergast, S. Banerjee, J. Phys. Chem. C 120 (2016) 23922–23932.
[61] M. Janousch, G.I. Meijer, U. Staub, B. Delley, S.F. Karg, B.P. Andreasson, Adv. Mater. 19 (2007) 2232–2235.
[62] T. Chakraborty, C. Meneghini, G. Aquilanti, S. Ray, J. Phys. Condens. Matter 25 (2013) 236002.
[63] E.P. Jahrman, L.A. Pellerin, A.S. Ditter, L.R. Bradshaw, T.T. Fister, B.J. Polzin, S. E. Trask, A.R. Dunlop, G.T. Seidler, J. Electrochem. Soc. 166 (2019) A2549–A2555.
[64] J. Zhou, L.T. Shan, Z.X. Wu, X. Guo, G.Z. Fang, S.Q. Liang, Chem. Commun. 54 (2018) 4457–4460.
[65] J. Wang, J. Polleux, J. Lim, B. Dunn, J. Phys. Chem. C 111 (2007) 14925–14931.
[66] L. Kong, C. Zhang, J. Wang, W. Qiao, L. Ling, D. Long, ACS Nano 9 (2015) 11200–11208.
[67] Q.S. Wang, Y.F. Zhang, H.M. Jiang, C.G. Meng, J. Colloid Interface Sci. 534 (2019) 142–155.
[68] W. Bi, Y. Wu, C. Liu, J. Wang, Y. Du, G. Gao, G. Wu, G. Cao, ACS Appl. Energy Mater. 2 (2019) 668–677.
[69] Y. Wang, J. Li, Z. Wei, J. Mater. Chem. 6 (2018) 8194–8209.
[70] Y.S. Cai, F. Liu, Z.G. Luo, G.Z. Fang, J. Zhou, A.Q. Pan, S.Q. Liang, Energy Storage Mater. 13 (2018) 168–174.
[71] Y.Q. Yang, Y. Tang, S.Q. Liang, Z.X. Wu, G.Z. Fang, X.X. Cao, C. Wang, T.Q. Lin, A. Q. Pan, J. Zhou, Nano Energy 61 (2019) 617–625.
[72] B.Y. Tang, J. Zhou, G.Z. Fang, F. Liu, C.Y. Zhu, C. Wang, A.Q. Pan, S.Q. Liang, J. Mater. Chem. 7 (2019) 940–945.
[73] G. Fang, J. Zhou, Y. Hu, X. Cao, Y. Tang, S. Liang, J. Power Sources 275 (2015) 694–701.
[74] H. Jiang, Y. Zhang, L. Xu, Z. Gao, J. Zheng, Q. Wang, C. Meng, J. Wang, Chem. Eng. J. 382 (2020) 122844.
[75] N. Zhang, M. Jia, Y. Dong, Y.Y. Wang, J.Z. Xu, Y.C. Liu, L.F. Jiao, F.Y. Cheng, Adv. Funct. Mater. 29 (2019) 1807331.
[76] T.Y. Wei, Q. Li, G.Z. Yang, C.X. Wang, J. Mater. Chem. 6 (2018) 8006–8012.
[77] J.W. Ding, Z.G. Du, L.Q. Gu, B. Li, L.Z. Wang, S.W. Wang, Y.J. Gong, S.B. Yang, Adv. Mater. 30 (2018) 1800762.
[78] C. Liu, S. Wang, C. Zhang, H. Fu, X. Nan, Y. Yang, G. Cao, Energy Storage Mater. 5 (2016) 93–102.
[79] B. Sambandam, V. Soundharrajan, S. Kim, M.H. Alfaruqi, J. Jo, S. Kim, V. Mathew, Y.K. Sun, J. Kim, J. Mater. Chem. 6 (2018) 3850–3856.